BROKEN CLOUD OBSERVATIONS AND PARAMETERIZATIONS FOR LONGWAVE RADIATION

By Zhaohui Cheng

Advisor: Professor Robert G. Ellingson

Scholarly Paper Submitted to the Department of
Meteorology in Partial Fulfillment of the
Requirements for the Degree of
Master of Science
August, 1999

Abstract

Clouds play a major role in regulating Earth s climate. However, computer models of Earth s climate include cloud effects in a primitive manner by assuming clouds to be flat the flat plate approximation. Cumulus clouds behave differently from flat plates because the vertical extent of the clouds shades more of the atmosphere and allow radiative exchange over a larger temperature range. To overcome the simplicity of GCMs but not to add too much computation, the effective cloud fraction is considered as a practical way to improve the plane-parallel theory. In this study, we use experimental data from a cloud radar, a lidar, and other observations to extract cloud information (coverage, thickness and aspect ratio) with which to test Ellingson s random cloud model. The extracted data are compared for consistency, and are used with radiation flux data to interpret the ability of the different techniques to infer cloud properties which are important to longwave radiative transfer under broken cloud conditions.

1. Introduction

Radiation is the fundamental process driving the global climate system. The balance between incoming solar radiation and outgoing infrared radiation largely determines the Earth's climate. Clouds play a major role in regulating the net radiative balance. For example, an increase in the average albedo of the Earth-atmosphere system of only 10% could decrease the surface temperature to that of the last ice age (NASA Climate Homepage, 1999). Hence small changes in cloud parameters may significantly amplify or offset climate feedback in GCMs.

The black, flat plate approximation is widely used in climate models for calculating cloud effects on radiation because it is computationally efficient. The recent advances in satellite remote sensing and three-dimensional radiative transfer have clearly demonstrated that the flat plate approximation in the presence of clouds is not valid over significant regions (Heidinger and Cox, 1996). As climate models begin to deal with the actual distributions of cloudiness, a detailed description of cloud three-dimensional geometry should be considered. The inclusion of the effects of cloud shadowing, channeling, cloud side radiation and cloud-cloud interaction becomes imperative, especially for broken cumulus clouds (Figure 1). The cloud geometry affects both

shortwave and longwave radiation. The present paper focuses on the geometrical effects of clouds on downwelling longwave radiation.

1.1 Background

Niylisk (1972) simulated the errors in longwave surface flux estimates from modified flat plate calculations. His results showed that the average error was roughly 20%. Ellingson (1982) studied the effect of cloud side emission. He analytically derived that cylindrically shaped cumulus resulted in more downward irradiance at the surface (1 to 4%) and less escaping the atmosphere (up to 8%) than from flat plate clouds. The subcloud layer experienced as much as 20% more heating than from flat plates, whereas the tropospheric column experienced up to 10% greater radiative cooling. Heidinger and Cox (1996) analyzed radiometer data collected in 1992 during the Atlantic Stratocumulus Transition Experiment (ASTEX) and found that if they ignored the vertical dimensions of the clouds, the longwave cloud radiative surface forcing was underestimated by 30%.

To overcome the simplicity of the flat plate approximation as a cloud-radiation model used in many GCMs, one might develop sophistical three-dimensional finite clouds and use Monte Carlo or three dimensional Eddington methods as the primary radiative transfer tools (Liou, 1992; Kobayashi, 1993). However, these methods are complicated and time-consuming within the framework of climate study. Instead, a practical and effective approach is to make a proper modification to the flat plate approximation. This modification is based on the understanding of the effects of broken cloud fields on atmospheric radiative transfer.

In most GCMs, longwave radiation quantities are often calculated as the cloud amount weighted average of the homogeneous clear and overcast conditions as:

$$Q = (1-N)\, Q_{clear} + N\, Q_{overcast}$$

Where Q is a radiation quantity such as flux, N is the cloud fraction and the subscripts clear and overcast denote the values for clear and overcast conditions.

A practical and time-saving approach to account for the effect of cumulus clouds in a one-dimensional scheme is to replace N with the effective cloud fraction N_e. Many researchers since Niylisk (1968, 1972) have focused on finite cloud parameterization to better estimate effective cloud fraction. Ellingson (1982) developed a model of a cumulus cloud field with the clouds parameterized as non-isothermal, black, random right circular cylinders. Harshvardhan and Weinman (1982) derived an empirical expression for the effective cloud fraction based on a numerical fit to the infrared radiative transfer through isothermal, regularly spaced, cuboidal clouds. Naber and Weinman (1984) tested a shifted periodic array of cuboidal clouds instead of the regular pattern. Killen and Ellingson (1994) used statistical spatial (Weibull and power law) and size (power law) distribution functions to calculate the effective cloud cover for broken cloud fields. They compared their results with previous studies and found that the effective fraction of broken clouds is not necessarily as great as previously predicted for simple shapes with regular or random arrays.

Takara and Ellingson (1996) used a Monte Carlo simulation to compute longwave scattering effects of broken clouds on fluxes and effective cloud fractions. Their results showed that the longwave scattering effects are significant in the 10 μm window region. More recently, Takara and Ellingson (1999) have found that scattering effects are negligible for liquid water clouds when water vapor absorption is accurately taken into account.

Heidinger and Cox (1996) developed a three-dimensional radiative transfer model to study finite cloud effects. The results indicate that, for optically thick clouds, the knowledge of cloud macrophysical properties can be more crucial than the detailed description of cloud microphysical properties to the modeling of longwave radiation transfer. Following previous work, Han and Ellingson (1999) developed a more generalized form of cloud geometrical effects on the effective cloud fraction. Comparisons among different model calculations reveal that cloud bulk geometrical shape, aspect ratio, size distribution and side inclination angle are the primary factors necessary to parameterize N_e. The spatial distribution becomes important for $N > 0.2$ and for large aspect ratios (> 0.5). Their results also show that for cases with large aspect ratio and cloud amount, there are large intermodel differences.

A small disparity in cloud cover can significantly alter the gradient and/or magnitude of longwave radiative properties. In turn this can affect cloud evolution and life span and ultimately influence climate. Errors of 0.15 in N can lead to flux errors at the surface of ~ $10 W/m^2$ and cooling rate errors in the free atmosphere of several °K/day (Han and Ellingson, 1999). Heidinger and Cox (1996) also showed that 0.1 errors in the observed values of N could cause flux errors of the same magnitude as those of Han and Ellingson (1999). Clearly, such errors are significant for climate studies. However, as noted above, the difference of N_e calculations for different models is larger, especially for large aspect ratios and cloud amounts (0.2-0.8). More precise N_e parameterizations are needed for climate modeling by GCMs. Precise observations of cloud geometrical features, size and spatial distributions are important to obtain better N_e parameterizations.

In this paper, the author attempts to use ground-based measurements at the Atmospheric Radiation Measurement (ARM) program (Stokes and Schwartz, 1994) Cloud and Radiation Testbed (CART) site in Oklahoma to derive absolute cloud fraction, cloud height, radius and many other variables characterizing cumulus clouds. The observed cloud data are used as input to the random cylinder model of Ellingson (1982). The calculated values of N_e are compared with values retrieved from observed fluxes. Han (1996) attempted the first validation of the form of the dependence of the effective cloud fraction on bulk cloud parameters using independently measured data at ARM CART. However, his test did not lead to a conclusion concerning the best model for cumulus clouds. In this paper, we make use of data from the Millimeter-Wavelength Cloud Radar (MMCR). Such measurements were not available for Han's analysis. Furthermore, several instruments used by Han have become more stable after several years' improvement. This study provides an extended analysis of the cloud model using new and perhaps improved measurements of the various model parameters.

In the material that follows, section 2 introduces the Ellingson random (1982) cumulus model and Han's (1996) N_e retrieval method. Section 3 describes details regarding the extraction of cloud variables. Section 4 tests the random model and discusses the latest MMCR radar data. The final section gives conclusions, discusses problems with the model and the observations, and, offers suggestions for future research.

2. Effective Cloud Fraction

As mentioned above, to overcome the simplicity of the flat plate approximation in GCMs, the effective cloud fraction has been proposed as a substitute for the flat plate

cloud fraction (the absolute cloud fraction). In this section we summarize the relationship of N_e to cloud properties as described by Ellingson's (1982) analysis, and then we describe the method to retrieve N_e from observed fluxes.

2.1 Random Cloud Model Description

Since our study mainly focuses on the downward longwave flux at the surface, we ignore cloud effects on the upward flux in the description.

Ellingson (1982) made four major assumptions concerning the atmospheric and cloud properties in order to derive his model, including:

- The atmosphere is plane parallel and horizontally homogeneous;
- The field of the cloud cover is homogeneous and isotropic;
- The height of the lower cloud boundary (cloud base) and the thickness of all the clouds in the system is the same; and
- The clouds are randomly distributed on the plane of the lower cloud boundary.

Defining $P_{clear}\downarrow(\theta)$ as the probability of the clear line of sight through the clouds to the surface at zenith angle θ, and $I_0\downarrow(z, \theta)$ and $I_p\downarrow(z, \theta)$ as the radiant intensities from the clear and cloudy areas of the sky, respectively, the flux $F\downarrow(z)$ may be written as

$$F\downarrow(z) = 2\pi \int_0^{\frac{\pi}{2}} P_{clear}\downarrow(\theta) I_0\downarrow(z,\theta) \sin\theta \cos\theta \, d\theta + 2\pi \int_0^{\frac{\pi}{2}} [1 - P_{clear}\downarrow(\theta)] I_p\downarrow(z,\theta) \sin\theta \cos\theta \, d\theta \quad (2.1)$$

Ellingson (1982) introduced the cloud relative height t as:

$$t = \frac{z' - z_{cb}}{z_{ct} - z_{cb}} = \frac{z' - z_{cb}}{h} \quad (2.2)$$

In the above equation, z' is an altitude between z_{cb} and z_{ct}, and h is the cloud thickness. P_{clear} was defined to satisfy the following conditions at the cloud boundaries:

$$P_{clear}\downarrow(\theta, t=0) = 1 - N, \qquad P_{clear}\downarrow(\theta, t=1) = P_{clear}\downarrow(\theta) \quad (2.3)$$

Ellingson (1982) assumed a linear variation of the cloud element radiance intensity with its relative height as follow:

$$I_p \downarrow (z,\theta,t) = I_p \downarrow (z,\theta,t=0)[1-\lambda \downarrow (z,h)t] \qquad (2.4)$$

Where $\lambda \downarrow (z,h)$, called the non-isothermality factor, is the ratio of the range of plate flux to the bottom plate flux:

$$\lambda \downarrow (z,h) = \frac{F_{pb} \downarrow (z) - F_{pt} \downarrow (z)}{F_{pb} \downarrow (z)} \qquad (2.5)$$

To simplify the equations, Ellingson(1982) gives a general form of N_e as:

$$N_e \downarrow = N + (1-N)[f \downarrow (N,\beta) - g \downarrow (N,\beta)\lambda \downarrow (z,h)] \qquad (2.6)$$

where

$$f \downarrow (N,\beta) = 2\int_0^{\frac{\pi}{2}} \sin\theta\cos\theta \int_0^1 \frac{1}{1-N}[-\frac{fP_{clear} \downarrow (\theta,t)}{f\,t}]dt \qquad (2.7)$$

$$g \downarrow (N,\beta) = 2\int_0^{\frac{\pi}{2}} \sin\theta\cos\theta \int_0^1 \frac{1}{1-N}[-\frac{fP_{clear} \downarrow (\theta,t)}{f\,t}]tdt \qquad (2.8)$$

In this study, the calculations neglect the non-isothermality factor (for display purpose). This allows N_e to be written as:

$$N_e \downarrow = N + (1-N) f \downarrow (N,\beta) \qquad (2.9)$$

Furthermore the probability of a clear line of sight from cloud sides at relative height t can be written as:

$$P_{clear}(\theta,t) = (1-N)\exp[tY(\theta)\ln(1-N)] \qquad (2.10)$$

By substituting eq.(2.10) into eq.(2.6) and (2.7), f (N, β) can be written as:

$$f(N,\beta) = 1 - 2\int_0^{\frac{\pi}{2}} \exp[\ln(1-N)Y(\theta)]\sin\theta\cos\theta\, d\theta \qquad (2.11)$$

Where Y(θ) represents the adjustment factor arising from the cloud sides. Assuming each cloud is a right-circular cylinder, Y(θ) can be written as:

$$Y(\theta) = \frac{2}{\pi}\beta \tan\theta \qquad (2.12)$$

2.2 Estimating N_e from Pyrgeometer Observations

A portion of this study is devoted to comparing observed estimates of N_e with model calculations using estimates of cloud thickness, absolute cloud fraction, and aspect ratio. Our estimates of N_e are based on a time coherence analysis of pyrgeometer observations of the surface downward flux following the work of Han (1996). For a single-layer cloud field, the downward longwave flux can be written as:

$$F\downarrow(z) = (1 - N_e)F_0\downarrow + N_e F_p\downarrow \qquad (2.13)$$

where F_0, F_p are the downward longwave flux for clear and cloudy skies respectively. So, N_e can be expressed as:

$$N_e = \frac{F\downarrow - F_0\downarrow}{F_p\downarrow - F_0\downarrow} \qquad (2.14)$$

This equation applies instantaneously to a large area compared to an individual cloud or to a single point when averaged over a time period sufficient to measure the equivalent spatial coverage. We obtain the fluxes in the equation (2.14) from observations, the details of which are discussed in the section 3.4.

3. Cloud Variable Extraction

3.1 Cloud Observation Instruments

The instruments used in this study are located at the ARM SGP CART site near Lamont, Oklahoma. The cloud observation instruments used here include the Millimeter-Wavelength Cloud Radar (MMCR), the Belfort Laser Ceilometer (BLC), the Micropulse

Lidar (MPL), and the Whole-Sky Image (WSI). A brief description of each is given below.

3.1.1 Millimeter-Wavelength Cloud Radar (MMCR)

The physical principle of Radar is that a pulse of electromagnetic energy is generated by the transmitter and propagated towards the cloud. When the electromagnetic wave intercepts the cloud droplets, it excites electromagnetic waves on the particles due to the change in the dielectic properties. Part of the energy propagated from the droplets is directed towards the surface where it is intercepted by a receiver. The primary function of radar is to measure the range and bearing of backscattering objects or "targets". Ranging is accoplished by a timing circuit that counts time between the transmission of a pulse and the reception of a signal. Generally radar uses millimeter radio waves as pulse.

Lidar has the same physical principle as that for Radar except it generally uses a more monochromatic wavelength focussed into a narrower beam. Lidar is able to detect cloud particles in locations when the lidar beam can penetrate to the location of the cloud particles. However, since the lidar used in this study uses visible light, its beam is subjected to large extinction during heavy overcast or with multiple cloud layers. This results in large errors in estimates of cloud properties.

In order to maximize sensitivity to cloud particles while reducing the effect of atmospheric attenuation on the radar beam, the zenith-pointing radar MMCR-operates at a wavelength of approximately 8.6 mm as compared to 0.523 μm for the lidar observations (Moran, 1997). Thus, the MMCR can detect cloud properties through heavy clouds, which may not be penetrated by a lidar. Since the MMCR can penetrate all cloud types, it s easy to detect multiple layers of clouds with the MMCR.

However, there are some problems with the MMCR data. When there are fairly high concentrations of very small drops at cloud base, the MMCR may not detect the cloud base. Insects also interfere with the MMCR operations. It is difficult to separate the cloud signal from the bug signal when both are present. Clothiaux, an MMCR expert at Penn State University, is trying to find techniques to solve the bug problem, but he still does not know how to remove the bug signature completely from the MMCR data (personal communication). We will see how this problem influences our results.

The MMCR data that are used herein were provided by Clothiaux (personal communication). He used several algorithms with the original observations to estimate cloud base, vertical distribution and thickness. Briefly, the MMCR collects data using a sequence of four modes. There are several systems within the radar that require calibration at regular intervals. The values obtained from these calibrations are stored as constants, polynomials, or curves in the calibration files or programs. Clothiaux's software converts the calibrated radar values to cloud base and top values in netCDF format. The data are obtained from 10-second averages of radar backscatter observations. The data provide the vertical distribution of the clouds and the cloud base and top height of each cloud layer.

3.1.2 Belfort Laser Ceilometer (BLC)

The Belfort Laser Ceilometer (BLC instrument homepage, 1999) is a lidar with the ability to detect and process several cloud-related parameters. These parameters include cloud height, extinction coefficient, cloud layers and time/date reference information. During normal operation, the ceilometer performs a data acquisition cycle

every 30 seconds. The field of view (FOV) is less than 3 milliradians and the valid cloud base is over a range of 15 meters to 7800 meters.

3.1.3 Micropulse Lidar (MPL)

The Micropulse Lidar (MPL instrument homepage, 1999) is a ground-based optical remote sensing system designed primarily to determine the altitude of clouds overhead. The physical principle is discussed above. The primary quantity obtained is the the lowest cloud base in meters, obtained from 60-second averages. The field of view (FOV) is about 0.1 milliradians and the valid cloud base is over a range of 27 meters to 15000 meters.

3.1.4 Whole-Sky Imager (WSI)

The Whole-Sky Imager (WSI instrument homepage, 1999) is an automated imager used for assessing and documenting cloud fields. The WSI is a ground-based electronic imaging system that monitors the upper hemisphere. It is a passive (non-emissive) system that acquires images of the sky dome through three spectral filters (neutral, red, and blue). From the WSI sky images, the ARM program has developed algorithms to assess the presence, distribution, shape and radiance of clouds over the entire sky. Compared to Radar and Lidar, the WSI has a full 180¡ field of view for viewing the complete sky dome simultaneously.

The WSI data analyses uses the so-called grey-scale "cloud decision" images taken at 10-minute intervals. Each pixel of the image has a grey-scale value ranging from 0 to 255 and indicates the sky status, such as background (0, 201-255), clear-sky (1-99) and cloudy (100-200) (Koehler and Shields, 1990). The WSI pixels with grey-scale values well below 100 are identified as clear-sky pixels. The grey-scale values of pixels

are small (below 100) if only cirrus clouds are present. However, the grey-scale values of cumulus cloud pixels are large (above 100). Thus WSI grey-scale values can be used to separate clear and cloudy sky, and exclude cirrus clouds.

3.2 Single Layer Cumulus Cloud Cases Selection

Our studies focus on single-layer cumulus cloud fields. By using single-layer clouds, we can neglect the variations in other layer clouds and cloud overlap. The data used in this research were obtained from the time period of April through June of 1997.

Times with single-layer cloud fields were determined by using Han s (1996) criteria, namely:

- The WSI grey-scale values of pixel are well above 100 for clouds.
- The MPL does not or rarely detects cirrus clouds during the observation period.
- The BLC observations indicate that the change in cloud base is below 5% of the mean and the cloud base is below 4km.

We introduce MMCR data as one of the criteria. Dividing the atmosphere into 10 layers between the surface to 20km, MMCR data provide the information within each layer. We estimate single layer cumulus clouds are present when:

- The WSI indicates cumulus clouds;
- The weather log shows broken clouds were reported on that day;
- The MMCR data show only the first layer (closest to the surface) has non-zero cloud bases and top heights; and
- The BLC and/or the MMCR show the cloud base is below 4km and it changes by <5% of the mean during the observation period.

In Han's (1996) research, no direct observations of cloud layers were available, and the WSI could not detect cloud overlap. Thus, Han s criteria mainly depend on the assumption of small fluctuations of a single layer cloud base. In this study, the MMCR can provide a more precise detection of a single cloud layer. By using the above criteria, 248 cases of single layer broken clouds were found during the period from April through June 1997.

3.3 Estimation of Cloud Model Parameters

Calculations of N_e for Ellingson (1982) model require cloud base (z_{cb}), cloud top (z_{ct}), absolute cloud fraction (N), cloud radius (R), cloud thickness ($h = z_{ct} - z_{cb}$), aspect ratio ($\beta = h/R$) and non-isothermal factor (λ). The techniques used to determine these variables are described below.

3.3.1 Cloud Base Height (Z_{cb})

z_{cb} can be determined either from the BLC or the MMCR observations. To correct the height difference between the height above the ground level and that of above sea level, the MMCR data have 315m subtracted from their original values. Recently, Clothiaux (personal communication) discovered that the correct base heights should be: $z_{cb} = z_{BLC}$ - 122m (applied in this study).

There are some differences between the MMCR and BLC cloud base heights. The lasers do not detect small concentrations of large drops. But large drops lead to very large radar reflectivities. Thus, in the presence of drizzle, the radar base will be lower than the laser-derived cloud base. Also, if there are fairly high concentrations of very small drops at cloud base with no drizzle passing through this region, the MMCR may not detect the

cloud base, but it may detect larger particles higher in the cloud. In this case, the laser-derived cloud base will be lower than the MMCR cloud base.

3.3.2 Cloud Top Height (Z_{ct})

We have used two techniques to extract cloud top heights. First, we directly extract the cloud top height from MMCR data. But sometimes, especially in summer, due to the effects of insects, it's hard to use the MMCR to determine the cloud top height. The only information that the MMCR can provide in those cases is the range of cloud top variations at that time.

The second method combines Han's techniques and MMCR data. With Han's method, z_{ct} is determined with the Balloon-Borne Sounding System (BBSS). The BBSS provides the vertical distribution of relative humidity (RH). According to Han (1996), z_{ct} may be estimated as the altitude of a layer, above z_{cb} that has the largest rate of RH decrease in the RH range of 65% - 75%. The steps we took to determine the cloud top are:

- Select the two soundings closest to the time of a single-layer cloud case;
- Estimate the cloud top for each sounding as noted above; then
- Interpolate cloud top height to the chosen case;
- Determine z_{ct} from the MMCR data; and
- Choose the smaller of the MMCR and BBSS cloud tops.

A comparison of the results from the two methods is discussed later in this paper.

3.3.3 Absolute Cloud Fraction

The absolute cloud fraction, N, is obtained using the return from the BLC and/or the MMCR using the ergotic principle following the work of Han (1996). This approach assumes:

- Clouds are distributed disalignedly and isotropically;
- In an interval T (10 min), clouds are advected over the instruments with constant speed U;
- The number of times clouds are observed is m;
- The sampling is done at intervals t_i (10s-MMCR ; 30s-BLC);
- The cloud projection on the ground surface is a square.

With these assumptions, N can be estimated as:

$$N = \frac{\left[\frac{1}{m}\sum_{i=1}^{m}(U \cdot t_i)\right]^2}{\frac{1}{m}U \cdot T} = \frac{\sum_{i=1}^{m} t_i}{T}$$

Following Han (1996), we use 10 minutes as the sampling time to extract N. Han (1996) pointed out that N follows the same tendency and agrees well from both 10 and 20 minutes samplings intervals. The sampling time is affected by many factors, such as the wind speed and the size and spatial distributions of the clouds. Since uncertainties in N_e are strongly tied to errors in N, N is a critical parameter. This study does not address such errors to a large extent. One of our recommendations will be to more seriously address this problem in further studies.

3.3.4 Average Cloud Effective Radius

We use the same assumptions as those used to estimate the N except that we assume the wind speed changes with the time. This study uses the radar wind profiler/RASS (RWP) to extract the wind speed. A brief description of this instrument follows below.

The radar wind profiler measures the wind profile from 0.1 km to 5 km and the virtual temperature profile from 0.1 km to 1.5 km. It operates by transmitting electromagnetic energy into the atmosphere and measuring the strength and frequency of backscattered energy. With the wind profiler data, we can extract the wind speed for different heights and times.

Based on the assumptions, the average detected segment length of a square L is given as: L = 0.71D = 1.42R, where D is the side length and R = D/2. Therefore, R = 0.70L. Using the BLC or MMCR observations, L is estimated as

$$L = \frac{1}{m} \sum_{i=1}^{m} u_i t_i$$

To estimate R, we had the same problem as for N—sampling time. We use 10 minutes here in order to be consistent with the extraction of the other variables.

3.3.5 The Non-isothermal Factor λ

If clouds grow tall, they cannot be treated as isothermal bodies. In this case, the non-isothermal factor, λ, has to be considered. As noted before, λ is the ratio of the flux range to cloud base flux. The non-isothermal clouds behave different from isothermal clouds on radiation transfer. When λ increases, N_e decreases (Han and Ellingson, 1999). λ approaches 0 for isothermal clouds. Following Han and Ellingson (1999), it is assumed that λ is linear with h. That is:

$$\lambda = \lambda_0 + k\,?h = \lambda_0 + k\,?(z_{ct} - z_{cb})$$

where λ_0 and k are constant. From Han (1996), λ_0 is close to 0 and k is close to $1.0\times10^{-4}m^{-1}$.

3.4 Cloud Radiation Observations

The CART pyrgeometer data give 1-minute flux averages at one-minute intervals. This flux cannot be used directly for the extraction of N_e because it is not representative of a spatially extended cloud field. As noted earlier, Equation (2.14) applies instantaneously over an area large compared to an individual cloud or for location averaged over a time period sufficient to measure the equivalent spatial coverage. In our case, the hemispheric flux observations are performed at a single site. We need to use the time domain to represent the space domain. We found that a 10-minute mean flux F↓, determined from 1-minute averaged fluxes, is best for the extraction of N_e, because it represents a relatively stable cloud pattern. The problem in estimating N_e from the pyrgeometer data then reverts to accurately determining F_o↓ and F_p↓.

There are three possible methods to obtain these variables.

- The first applies a temporal coherence technique to the pyrgeometer data. Since the pyrgeometer has a large field of view. It is rare for the pyrgeometer to observe a completely clear or overcast sky during a time period when broken clouds are dominant. Thus, obtaining accurate estimates of the F_0↓ and F_p↓ from pyrgeometer observations is difficult by this technique.
- The second method uses observations from the ground-based Atmospheric Emitted Radiance Interferometer (AERI) to estimate F_0↓ and F_p↓. There is a high likelihood of obtaining a more correct representation of the clear- and cloudy-sky radiances (I_0↓

and $I_p\downarrow$) with the AERI, because the AERI has a small field of view (FOV, 0.86°). The AERI data are reported at approximately 8-minute intervals.

The technique for converting radiances to fluxes was proposed by Ellingson and Wiscombe (1996). The fundamental principle of this technique comes from the fact that for a given plane parallel, horizontally homogeneous atmosphere, both the vertically downward longwave radiance and the downward longwave flux are governed by the same temperature and gaseous absorbers (i.e., water vapor, carbon dioxide and ozone) (Ellingson, 1995). Ellingson and Wiscombe (1996) showed that the downward AERI-based flux at the surface, $F\downarrow$, may be related to the vertically downward radiance, $I^{obs}\downarrow(1)$, in the form

$$F \downarrow = I^{obs} \downarrow (1) ? L \qquad (3.1)$$

where the anisotropic factor, L, is expressed as:

$$L = \frac{2\pi \int_0^1 I^{obs} \downarrow (\mu) \mu \, d\mu}{I^{obs} \downarrow (1)} \cup \frac{2\pi \int_0^1 I^{cal} \downarrow (\mu) \mu \, d\mu}{I^{cal} \downarrow (1)} \qquad (3.2)$$

where μ is the cosine of the zenith angle and the superscripts obs and cal represent observed and calculated, respectively. It is assumed that the model calculates the relative angular variation of the radiance field more accurately than the absolute radiances. Thus L can be obtained from an atmospheric radiation model using radiosonde data as input (Han, 1996).

At the ARM SGP CART site, the AERI instrument measures the downward infrared spectral radiance emitted by the atmosphere in the range 550-3020 cm^{-1} with a spectral resolution of 0.5 cm^{-1}. No measurements are performed for the

wavenumber region of 0-550 cm^{-1}. As a substitute, the AERI flux in this study is estimated as

$$F \downarrow = F_{0-550} \downarrow + I^{obs}_{550-3020} \downarrow (1) ? L \qquad (3.3)$$

where the spectral flux $F_{0\text{-}550}\downarrow$ is calculated from a radiation model or the Planck function, and L can be estimated from equation (3.2) for the 550 - 3020 cm^{-1} interval. We use Planck function to calculate $F_{0\text{-}550}\downarrow$ in this study.

The extracted mean $I_0\downarrow$ and $I_p\downarrow$ can be converted to $F_0\downarrow$ and $F_p\downarrow$ using equation (3.3).

- The third method involves the use of a radiation model with atmospheric sounding data to calculate $F_0\downarrow$ and $F_p\downarrow$. The model calculations can compensate for the absence and weakness of AERI observations. This occurs because the AERI sometimes was not in operation during a specific time period, and when the cloud coverage is small or large, it s hard for AERI to detect a completely cloudy or clear area.

We adopt the Warner-Ellingson (1999) model for the calculation of downward longwave radiances and fluxes at the surface, as this model is derived from the line-by-line model LBLRTM (Clough et. al., 1992) that shows good agreement with AERI observations.

3.5 Downward Longwave Fluxes Validation

Since we are using different observations for the various fluxes in equation (2.14), we must account for systematic differences between the AERI ($F_{aeri}\downarrow$), the pyrgeometer ($F_{pyr}\downarrow$) and the random model calculations ($F_{mod}\downarrow$) under homogenous clear and cloudy skies.

To estimate systematic differences, 25 clear-sky cases and 22 overcast cases were found during research period (April — June, 1997). Table 1 gives the mean differences of fluxes and their standard deviations for both clear and overcast conditions. The mean AERI-pyrgeometer differences for those periods are less than or close to 1% of the mean AERI flux.

Table 1 The mean differences and their deviation between various fluxes under clear- and overcast-sky conditions

	Clear-Sky Cases (25)		Overcast-Sky Cases (22)	
	Mean (W/m^2)	Std (W/m^2)	Mean (W/m^2)	Std (W/m^2)
$F_{aeri}\downarrow - F_{pyr}\downarrow$	-3.86	2.34	-1.71	1.54
$F_{pyr}\downarrow - F_{mod}\downarrow$	6.48	4.04	2.47	2.39
$F_{aeri}\downarrow - F_{mod}\downarrow$	2.62	2.46	-0.77	2.02

Figure 2 and 3 show histograms of $F_{aeri}\downarrow - F_{pyr}\downarrow$, $F_{pyr}\downarrow - F_{mod}\downarrow$, and $F_{aeri}\downarrow - F_{mod}\downarrow$ under clear-sky and overcast—sky conditions respectively. The figures show that the discrepancies among these three data sets all fall near the 1% of AERI accuracy range, meaning very good agreements among them. However, the differences also show that there are systematic departures among the measurement results and model calculation. Assuming the AERI observations are the best, equation (2.14) can be rewritten as:

$$N_e = \frac{F_{pyr}\downarrow - 2.78 - F_{aeri}(clr)\downarrow}{F_{aeri}(cld)\downarrow - F_{aeri}(clr)\downarrow}$$

Since in this study many clear- and overcast-sky fluxes can not be observed directly by the AERI under broken cloud conditions, fluxes calculated by the Warner-Ellingson (1999) are used whenever AERI observations are not available. Thus, the most important systematic discrepancy comes from the difference between the pyrogeometer observations and the model calculations. Assuming $F_{pyr}\downarrow$ is more accurate, we can correct these systematic deviations to accurately estimate N_e by the equations below:

$$N_e = \frac{F_{pyr} \downarrow - F_{\mathrm{mod}}(clr) \downarrow - 6.48}{F_{\mathrm{mod}}(cld) \downarrow + 2.47 - F_{\mathrm{mod}}(clr) \downarrow - 6.48}$$

The subscript clr and cld mean the clear and overcast-sky.

4. Discussion and Results

The various ARM SGP CART observations discussed above were used to determine the model parameters N, R, H and β. With these parameters, N_e for the random cumulus model was calculated. And N_e was also retrieved from the downward longwave fluxes observations as described above. In this section we will discuss the differences between the BLC and MMCR estimated cloud parameters, and we will compare pyrgeometer-retrieved N_e with N extracted from the BLC and with values calculated from the random cumulus model equations.

4.1 Comparison Between MMCR and BLC (N and R)

Shown in Figures 4 and 5 are the number distributions of cloud radius (R), absolute cloud fraction (N), cloud thickness (h), and aspect ratio (β) derived from the BLC and the MMCR, respectively. The BLC cloud radii (Fig. 4a) shows the clouds to be of the order of 500 to 1000 m in horizontal extent, whereas the MMCR-derived cloud radii tend to be larger. The MMCR-derived clouds' horizontal extent is concentrated about 1000-1500 m. MMCR-derived radii larger than 2000 m occupy almost 20% of the 248 cases, whereas the same range is found in only 6% of the total in BLC data. We can see the difference between BLC and MMCR radii clearly in Figure 7c. Generally the MMCR cloud radius is greater than the BLC by about 600 m.

As regards the absolute cloud fraction, Figure 4(b) shows the BLC cloud fraction is generally less than 0.5, whereas Figure 5(b) shows at least half of the MMCR cloud fractions fall into the range larger than 0.5. Figure 7a and b show the ratio of MMCR to

BLC cloud fraction as a function of BLC cloud fraction and radius respectively. The MMCR cloud fraction exceeds the BLC value by more than a factor of 2 for $N < 0.3$. The MMCR cloud fraction becomes close to the BLC value for large N (7a). Overall, the MMCR and BLC cloud fractions tend not to be close until the cloud side-length reaches about 1500m (Fig. 7b).

Why are there large differences between the variables extracted by the BLC and MMCR? One possible reason is the different instrument sensitivity to cloud properties. As mentioned above, the lasers do not detect small concentrations of large drops, but large drops lead to very large radar reflectivities. This will cause the MMCR to have a greater chance of detecting a cloud, and, this will lead to a greater cloud fraction and radius.

The different sampling intervals and view cross section of these two instruments may also lead to differences. The sampling interval is 10s and 30s for the MMCR and BLC, respectively. The time sampling difference can account for at most a 400 m difference in R for a 10m/s wind speed. When the data are filtered to include only those samples with $| R_{MMCR} - R_{BLC} | \leq 400$ m, there is a considerably improved agreement in N's (Fig. 8a) and the aspect ratio (β) (Fig. 8b).

However, the MMCR cloud radii are generally much larger than the BLC's (Fig. 7c). This large difference may be explained by the "insect/atmospheric plankton" problem. Since the single layer cumulus cloud fields often occur in the spring and summer, we selected the cases in the period from April to June 1997. But this is also the period when insects cause significant problems with the radar observations. As mentioned earlier, it's difficult to differentiate the signal from insects from that of the

clouds. Thus, if we interpret the bug signal as a cloud signal, both N and R will be biased toward large values.

4.2 Cloud Thickness *h* and Aspect Ratio β: Comparison Between Observations From the MMCR and Radiosondes

Cloud thickness is defined as $h = z_{ct} - z_{cb}$. As noted in section 3.3, cloud base height z_{cb} can be extracted directly from the MMCR or BLC observations. To retrieve the cloud top height, two methods were introduced in section 3.3. However, up to now, there has not been a good way to estimate cloud top.

Fig. 4c and 5c are the histograms of radiosonde-BLC and MMCR cloud thicknesses respectively. It is clear that the MMCR detects much thicker clouds. The most frequent MMCR-observed cloud is about 700m thick, and about 12% of the MMCR-observed clouds have thicknesses greater than 2500m (5c). The radiosonde-estimated thicknesses (4c) show no clouds thicker than 2000m for the selected cases. The most frequent radiosonde thickness is about 400m, and about 85% of the cloud thicknesses are from 300m to 1200m. Figure 7d shows linearity between the two estimates, but the MMCR thicknesses exceed the BLC-sonde estimates by about a factor of 1.5.

The aspect ratio β is defined as h/R. Figures 4d, 6 and 5d show the number distribution of aspect ratios computed as h_{MMCR}/R_{BLC}, h_{sonde}/R_{BLC} and h_{MMCR}/R_{MMCR}, respectively. Due to the large radii measured by the MMCR, the MMCR-derived β's are smaller than those derived from the BLC-radiosonde data. About 85% of the MMCR β's are less than or equal to 1.0 and the peak is 0.3. Using the BLC-radiosonde data for the

same cases, the aspect ratios from 1.0-1.5 occupy 40% of the total, and a second peak occurs at 1.3.

We also calculated aspect ratios with the MMCR derived thicknesses and the BLC derived radii (Fig 4d). The aspect ratio ranges from 0.3 - 2.5, which is much larger than those derived from only the MMCR data (Fig. 5d). More than 40% of the cases have aspect ratios from 1.5 to 2.5. Up to now, we had not been able to judge which aspect ratio was more reliable because we could not obtain accurate information about the cloud top. We expect that algorithms that use satellite observations or better cloud radar/or lidar data could yield better estimates for the cloud top heights and for cloud aspect ratios.

4.3 Effective Cloud Fraction: Comparison between Observation and Model Calculation

Based on the ground-based measurements at the SGP CART site during period of April to June in 1997, the various cloud variables have been estimated for 248 cases of single-layer cumulus cloud fields. Figure 9a shows the differences between the pyrgeometer-retrieved N_e [N_e(retr)] and BLC-estimated N for different β ranges, where β is derived from the MMCR thicknesses and the BLC radii. The Model values are shown as lines for the indicated β's. For the BLC data, N_e(retr) is larger than N. The relationship between the retrieved N_e and N indicates that the effect of bulk geometry of cumulus clouds is to make N_e significantly different from the flat plate cloud coverage. The agreement with the random model is spotty, particularly for large β and small N. In fact, the contribution of cloud sides on N_e is mainly in the 0.2 — 0.8 range of N. The author believes that the large disparities between model and retrieved N_e-N at small N ($N<0.2$) are due to observational errors in the fluxes and N. But the results in the 0.2 - 0.8 range of

N are encouraging. Han(1996) showed much better agreement using β's determined from BLC and radiosonde data. The author also obtains better results when using the BLC-radiosonde β's (Fig. 9b).

Different model input parameters will cause a dispersion between model calculated N_e's. Figure 10 shows the different effects of parameters derived from the MMCR, the BLC, and the radiosonde data on model calculations of N_e. Fig. 10a shows differences between modeled Ne's for different input N's using the sameβ. In general, the N_e differences are linear in the differences in N, for different N's, the model yields large) N_e's, and the average difference is 0.287 for all cases.

Fig. 10b shows the effects of different radii on modeled N_e's keeping h and N constant. Again,) N_e is linear in) R, and the mean difference is -0.054, which is about 19% of the effect of N. Compared with the effects of N and R, the thickness effect is smallest (Fig. 10c, N and R are identical for each set). The mean N_e difference is -0.038, which is much smaller than that from N and R. Thus, errors in N and R are the major sources of error in N_e in this study. Obviously, accurate N is the most important factor for calculating N_e. In this study, the results show that the MMCR data yield large differences in N and R relative to the BLC and to the pyrgeometer. Thus, the MMCR data do not appear to be as useful as we expected for cloud geometry description, especially in spring and summer season. Nonetheless the data are powerful for cloud layer analysis and case selection.

There are also several other factors besides N and β that will affect the calculation of N_e. These parameters include cloud shape, the non-isothermal factor, side inclination angle, and the size and spatial distributions. Due to the limitations in current cloud

observations, we do not have sufficient data to provide all the parameters necessary for the N_e model used herein. Figure 11 shows the difference between pyrgeometer retrieved and model calculated N_e as function of N and β, respectively. The model calculated N_e's in Figure 11(a) and (b) are different from those in Figure 11(c) and (d) because different β's are used as input. There is a quasi-linear trend of the difference from negative to positive with increasing N or β. This result shows that the model calculated N_e is less than the pyrgeometer retrieved N_e [N_e(retr)] for small N (or/and small β), but, it is greater than N_e(retr) for large N (or/and large β). These differences could come from the simplicity of the model-input parameters. However, we ignored the inclination angle and the size distribution factor in the model used in this study. If one used the more general model of Han and Ellingson (1999), with a size distribution factor of v = 2.5, the center of N_e-N maximum will shift to smaller N (0.25-0.3) as compared to the current center location (N ~ 0.4). This would improve the comparisons of the observations with the calculations.

5. Summary

In order to allow GCMs to include the effects of broken cloudiness without significantly increasing computation, the effective cloud fraction has been proposed as a replacement to the absolute cloud fraction in one-dimensional longwave radiative transfer calculations. Improvements to N_e parameterizations require tests of current schemes with observations. Following Han's (1996) work, we use ground-based measurements from the ARM SGT CART site to estimate cloud variables characterizing cumulus clouds. With an empirically determined sampling period of 10 minutes, these measurements were used to extract the effective cloud fraction, absolute cloud fraction and many other variables

characterizing cumulus clouds. Overall, 248 single-layer cumulus cloud cases were found. We discussed the differences between BLC and MMCR estimated cloud variables, and compared pyrgeometer-retrieved N_e with N extracted from BLC and with values predicted by the random cumulus model.

In the few studies since the pioneering work by Han (1996), new and/or improved ARM data streams have become available that allow a more detailed test of N_e models. In particular, this study makes use of data from a cloud radar (MMCR), a wind profiler and an improved interferometer (AERI). These additions are important because:

- The MMCR allow, theoretically, a simple identification of single layer clouds and cloud boundaries;
- The wind speeds from the wind profiler allow more accurate calculations of cloud sizes; and
- The corrected AERI data allow more accurate clear and overcast flux estimates.

The major findings from the analyses described herein are:

- Cloud fractions and side-lengths derived from the BLC and MMCR using the ergotic assumption show larger than expected differences;
- Preliminary analyses of the pyrgeometer data suggest the BLC-derived parameters are more consistent with the pyrgeometer and cloud-radiation model than are the MMCR values;
- The difference between the MMCR and BLC cloud fractions are the primary cause for the large disparity of the N_e calculations;

- The difference between the MMCR and BLC cloud property estimates are likely due to different instrument sensitivities to the cloud microphysical properties, different sampling times, and possibly to atmospheric plankton.

Clarifying these issues is key to future use of the MMCR in ascertaining more than cloud bottom and top boundaries in studies of broken cloud effects on longwave radiation. Some additional cloud microphysical properties should be considered in model to better parameterize the N_e.

Additional research is needed to test N_e parameterizations. In particular, the following might prove useful:

- Better estimates of N and R may depend on a more precise determination of an accurate sampling time. It may be possible to determine a more appropriate sampling time for broken clouds conditions using Monte Carlo models for a range of cloud shapes and different spatial and size distributions;
- Use of the WSI to estimate N. The WSI can be used to estimate the cloud fraction at zenith. Comparisons of these cloud fractions with those from the MMCR and BLC are needed to further test the ergotic assumption and areal fraction;
- Use of satellite data to estimate the cloud top heights;
- Use of an array of cloud radars/lidars to directly measure the cloud shape, spatial and size distributions.
- Use of the microwave radiometer (MWR) to filter the MMCR and BLC data. The MWR measures the liquid water path (LWP). It may be possible to set a threshold for LWP that defines when clouds are important to both longwave radiation AND the radar reflectivity.

References

Belfort Laser Ceilometer (BLC) instrument homepage, 1999: http://www.arm.gov/docs/instruments/static/blc.html.

Clough, S. A., M. J. Iacono, and J. -L. Moncetm, 1992: Line-by-line calculations of atmospheric fluxes and cooling rates: Application to water vapor. *J. Geophp. Res.*, **97**, 15761-15785.

Ellingson, R.G., 1982: On the effects of cumulus dimensions on longwave irradiance and heating rate calculations. *J. Atmos. Sci.,* **39**, 886-896.

—, 1995: Surface longwave fluxes from satellite observations: A critical review. *Remote Sens. Environ.*, **51**, 89-97.

—, W. J. Wiscombe, 1996: The spectral radiance experiment (SPECTRE): Project description and sample results. *Bull. Amer. Meteor. Soc.*, **77**, 1967-85.

Han, D. J., 1996: Studies of longwave radiative transfer under broken cloud conditions: cloud parameterizations and validations. *Ph. D. Dissertation*, University of Maryland, College Park, 1-163.

Han, D. J., and R. G. Ellingson, 1999: Cumulus cloud formulations for longwave radiation calculations. *J. Atmos. Sci.,* **56**, 837-851.

Harshvandhan, and J. A. Weinman, 1982: Infrared radiative transfer through a regular array of cuboidal clouds. *J. Atmos. Sci.,* **39**, 431-439.

Heidinger, A. K., and S. K. Cox, 1996: Finite-Cloud effects in longwave radiative transfer. *J. Atmos. Sci.,* **53**, 953-963.

Killen, R., and R. G. Ellingson, 1994: The effect of shape and spatial distribution of cumulus clouds on longwave irradiance. *J. Atmos. Sci.,* **51**, 2123-2136.

Kobayashi, T., 1993: Effects due to cloud geometry on biases in the albedo derived from radiance measurements. *J. Climate,* **6**, 120-128.

Koehler, T., and J. Shields, 1990: Factors influencing the development of a short term CFARC prediction technique based on WSI imagery. Technical Note 223, Marine Physical Laboratory, SCRIPPS Institution of Oceanography, San Diego, CA, 92151-6400.

Liou, K. N., 1992: *Radiation and cloud processes in the atmosphere: theory, observation, and modeling.* New York: Oxford, 1-461.

Micropulse Lidar (MPL) instrument homepage, 1999: http://www.arm.gov/docs/instruments/static/mpl.html.

Millimeter Wave Cloud Radar (MMCR) instrument homepage, 1999: http://www.arm.gov/docs/instruments/static/mmcr.html.

Moran, K. P., B. E. Martner, D. C. Welsh, D. A. Merritt, M. H. Post, and T. Uttal, 1997: *ARM s cloud-profiling radar. 28th Conf. on Radar Meteorology,* Austin, TX, Am. Metor. Soc., 296-297.

Naber, P. S., and J. A. Weinman, 1984: The angular distribution of infrared radiances emerging from broken fields of cumulus clouds. *J. Geophys. Res.,* **89**, 1249-1257.

NASA Climate Homepage, 1999: http://climate.gsfc.nasa.gov/index.html.

Niylisk, Kh., 1972: Cloud characteristics in problems of radiation energetics in the earth s atmosphere. *Izv. Acad. Sci. USSR, Atmos. Oceanic Phys.,* **8**, 270-281.

, 1968: Atmospheric thermal radiation in partly cloudy regions. *Atmos. Oceanic Phys.,* **4**, 383-396.

Stokes, G. M. and S. E. Schwartz, 1994: The atmospheric radiation measurement (ARM) program: programmatic background and design of the cloud and radiation test bed. *Bull. Ameri. Meteor. Soc.*, **75**, 1201-1221.

Takara, E. E., and R. G. Ellingson, 1996: Scattering effects on longwave fluxes in broken cloud fields. *J. Atmos. Sci.,* **53**, 1464-1476.

and R. G. Ellingson, 1999: Broken Cloud Field Longwave Scattering Effects. *J. Atmos. Sci.,* **56**, In press.

Warner, J. Y., and R. G. Ellingson, 1999: A new longwave model for application to atmospheric problems. *J. Atmos. Sci.*, **56**, In press.

Whole-Sky Imager (WSI) instrument homepage, 1999: http://www.arm.gov/docs/instruments/static/wsi.html.

The Plane Parallel Cloud Assumption Underestimates Cloud Cover at all View Angles > 0°

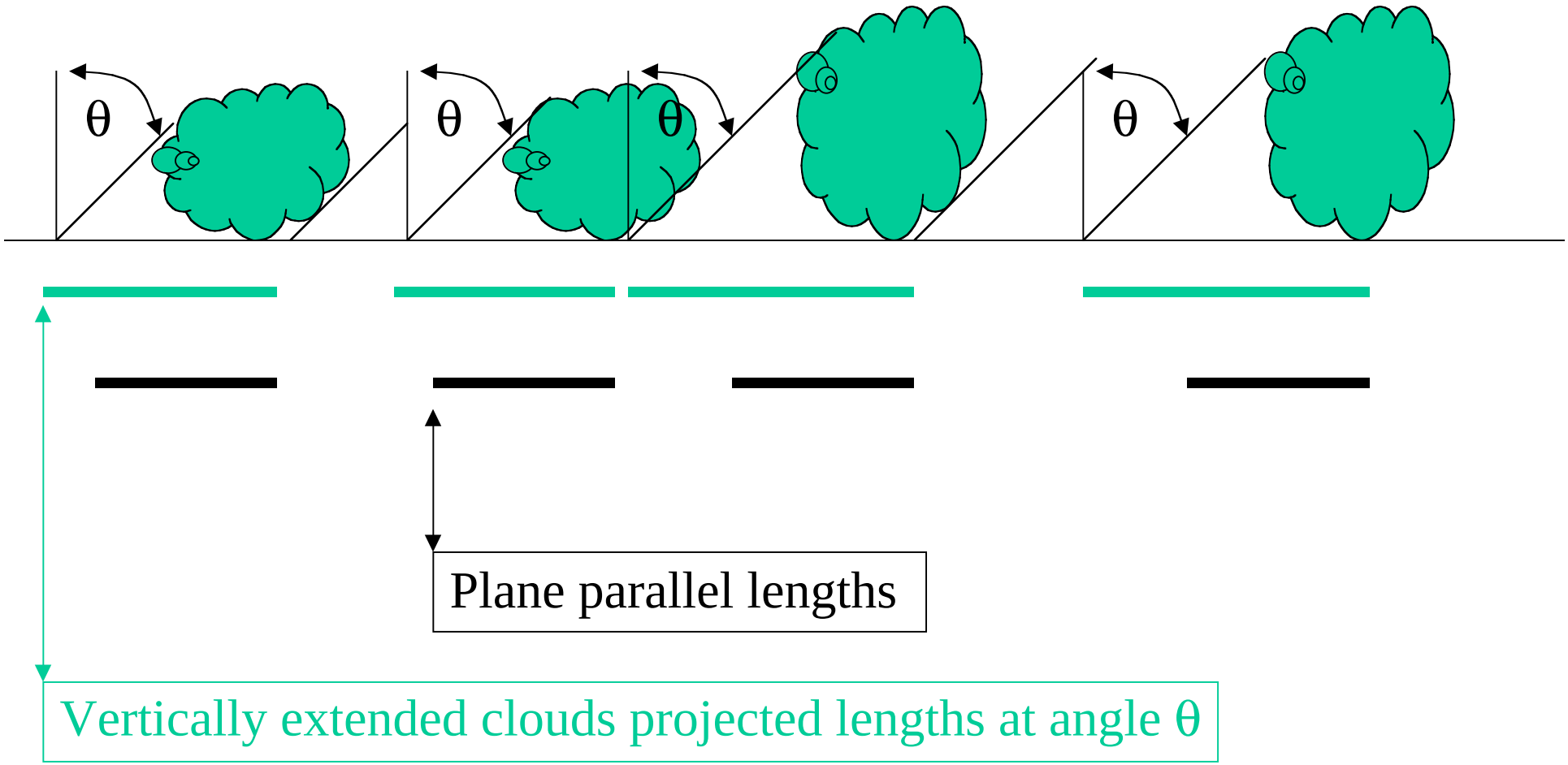

Fig. 1. The side-length effect of vertically extended clouds on cloud cover.

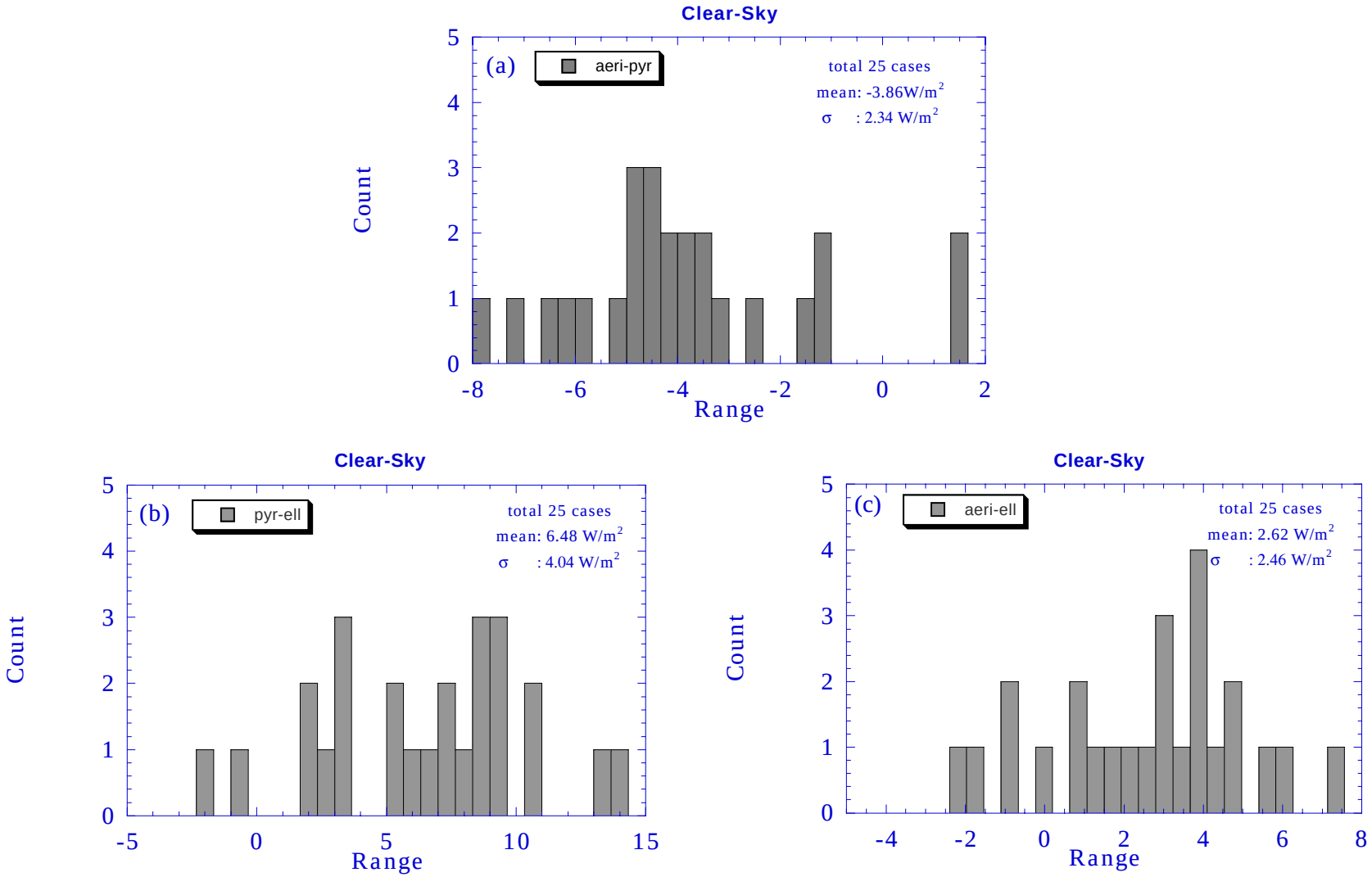

Fig. 2. Histograms of (a) AERI-pyrgeometer, (b) pyrgeometer-model, and (c) AERI-model fluxes for clear-sky cases.

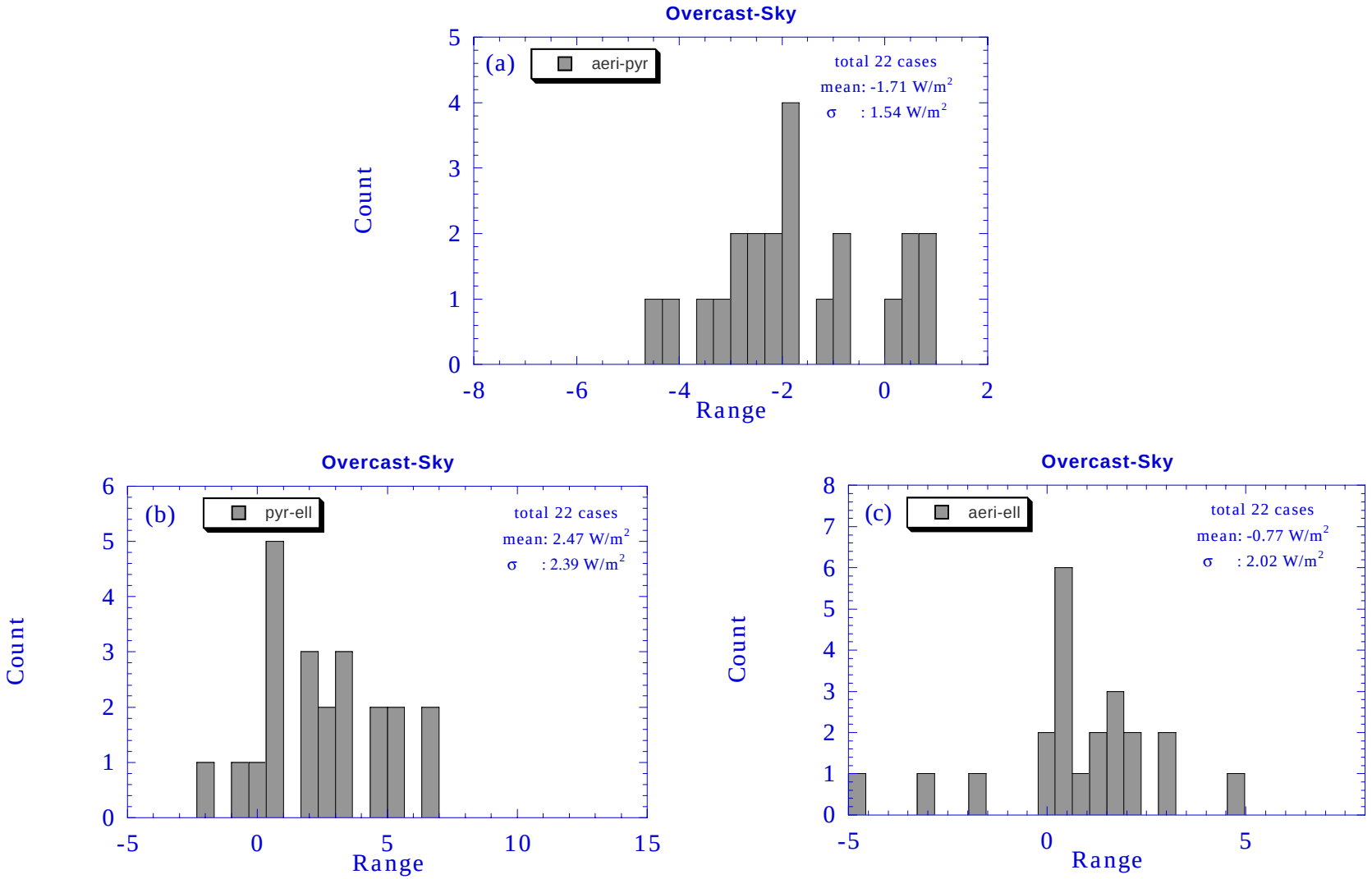

Fig. 3. As in Fig. 2, but for the overcast cases.

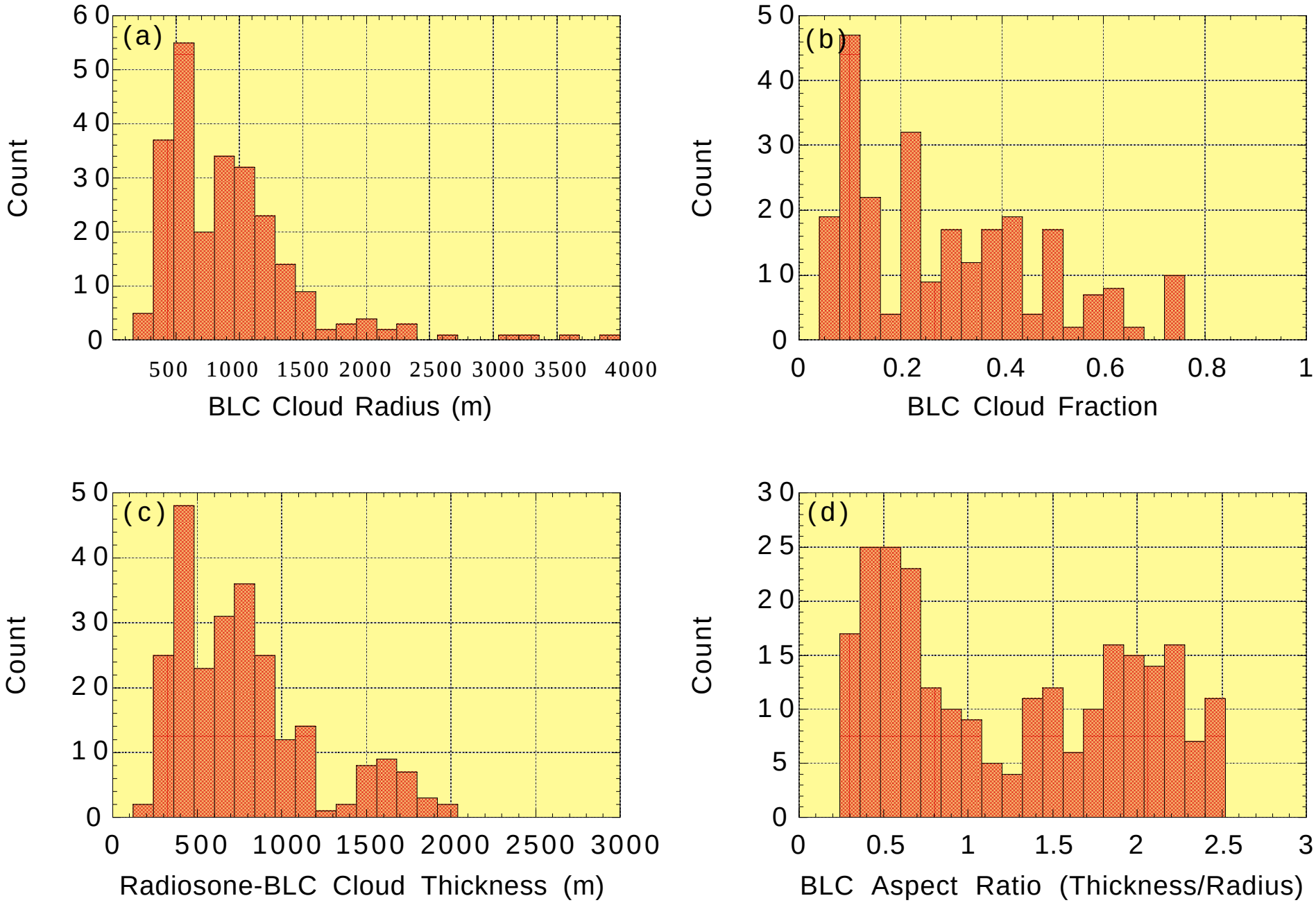

Fig. 4. Number distributions of BLC derived quantities: (a) cloud radii, (b) absolute fraction, (c) thickness, and (d) aspect ratio.

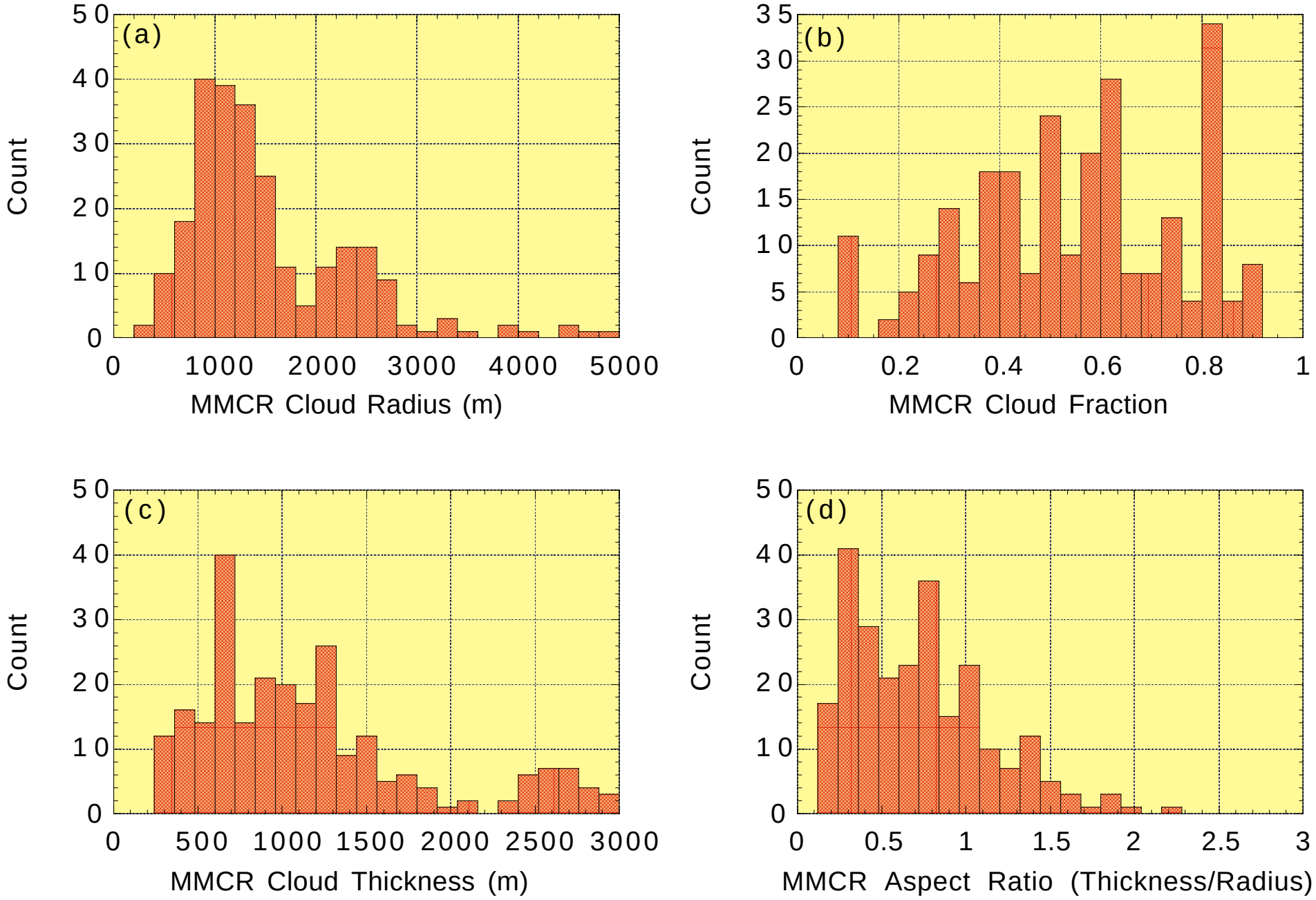

Fig. 5. As in Fig. 4, but for the MMCR.

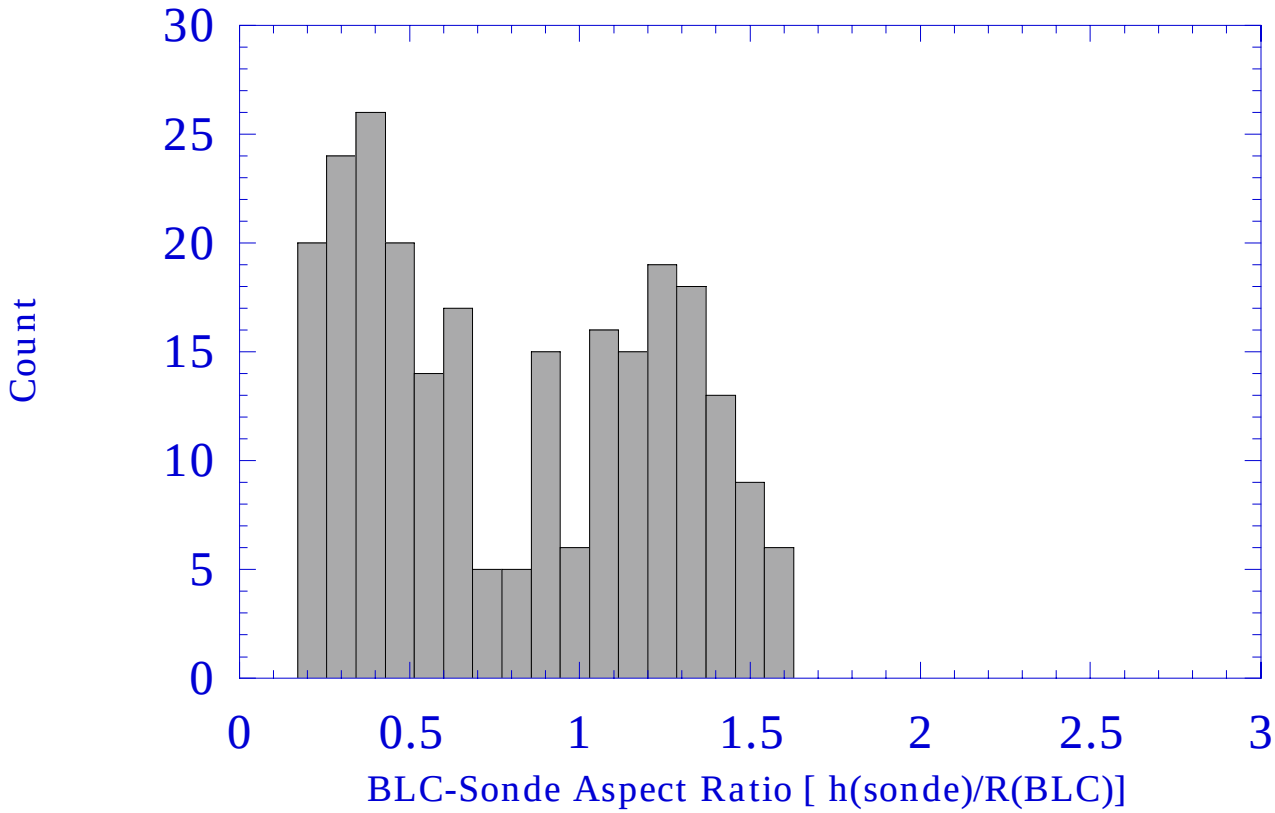

Fig. 6. Number distributions of BLC-Sonde derived aspect ratios.

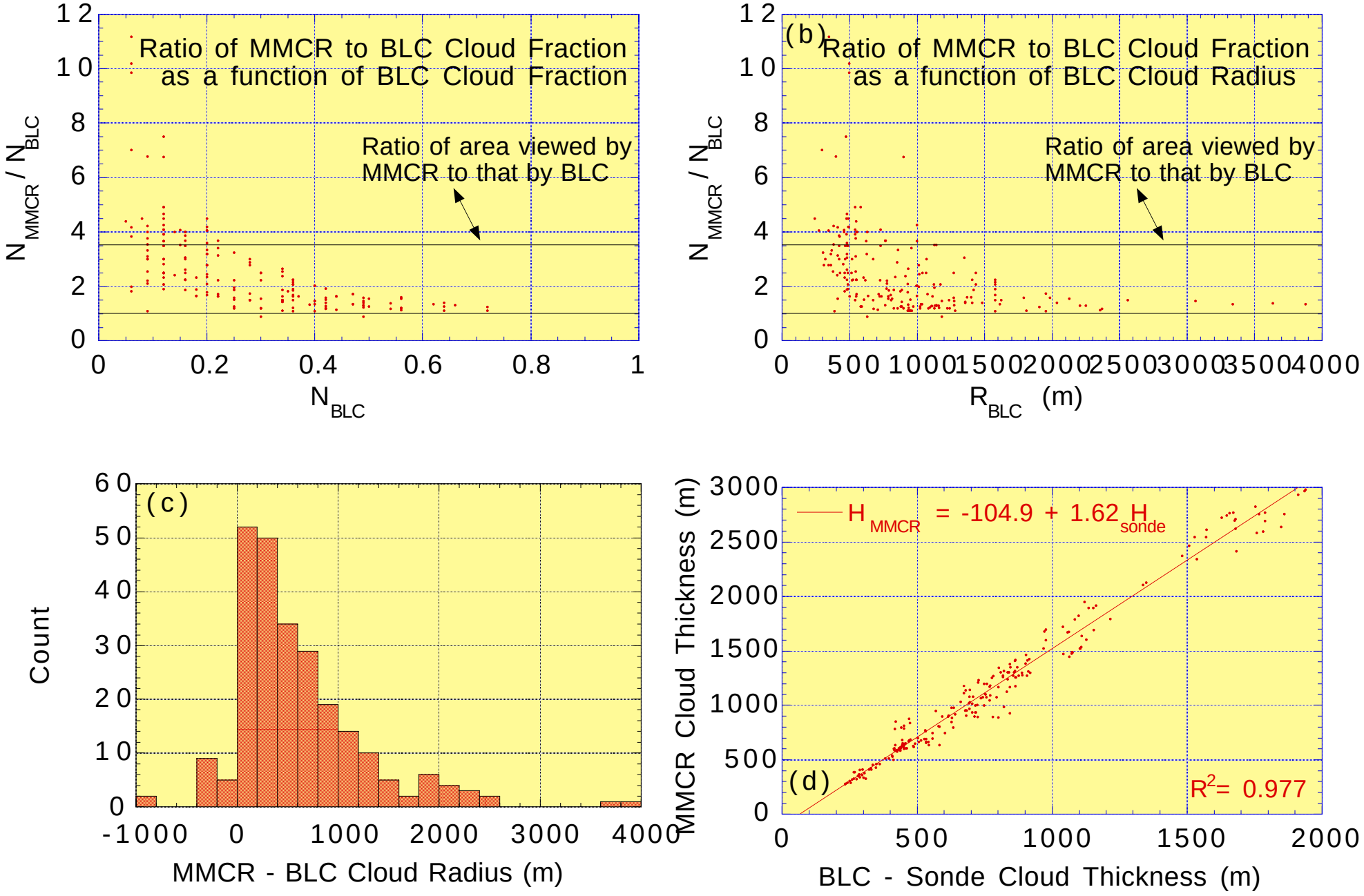

Fig. 7. Ratio of MMCR to BLC cloud fraction as functions of (a) NBLC, and (b) BLC cloud radius. (c) Number distributions of MMCR-BLC cloud radii, and (d) MMCR and BLC-sonde cloud thickness relationship.

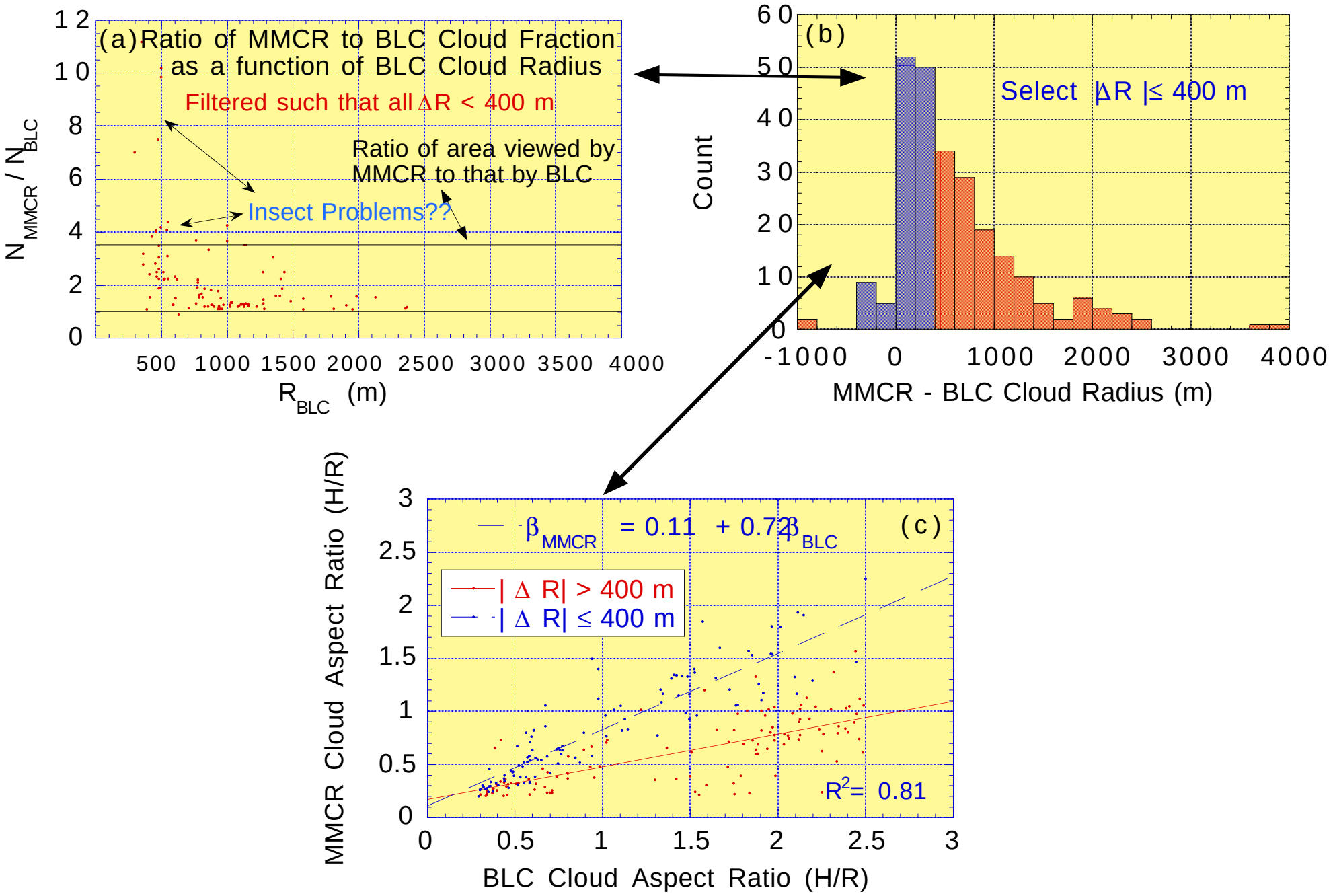

Fig. 8. (a) Ratio of MMCR to BLC cloud fraction as a function of BLC cloud radius; (b) distribution of the MMCR-BLC radii differences; and (c) relationship between MMCR and BLC determined aspect ratios.

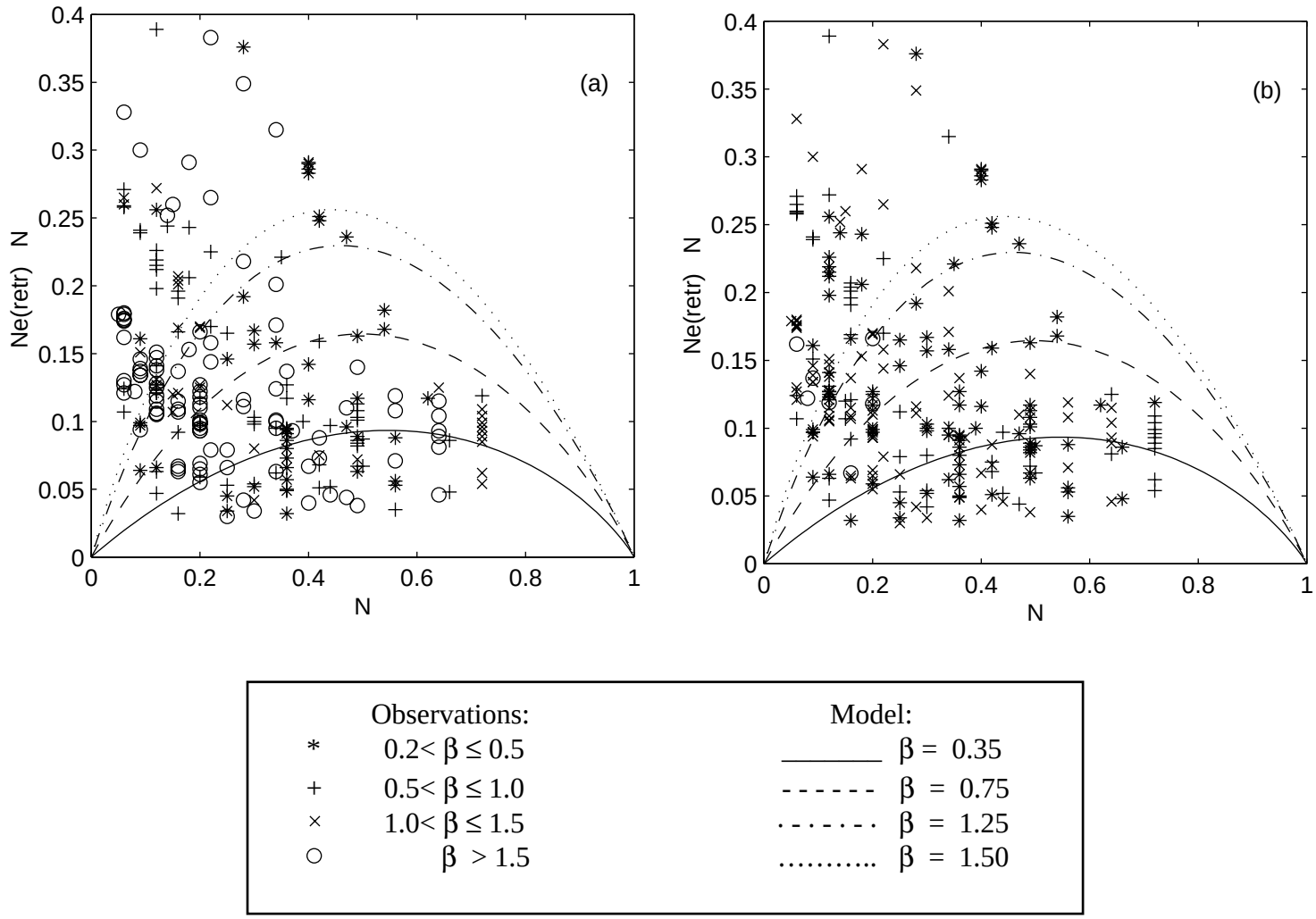

Fig. 9. Differences between the effective cloud fractions retrieved from the pyrgeometer (Ne(ret)) and the absolute cloud fractions obtained from the BLC for different range of the aspect ratio - (a) β=h(MMCR)/R(BLC) and (b) β=h(sonde)/R(BLC). Shown with the lines are theoretical model calculations for randomly distributed cylinders with the indicated β's.

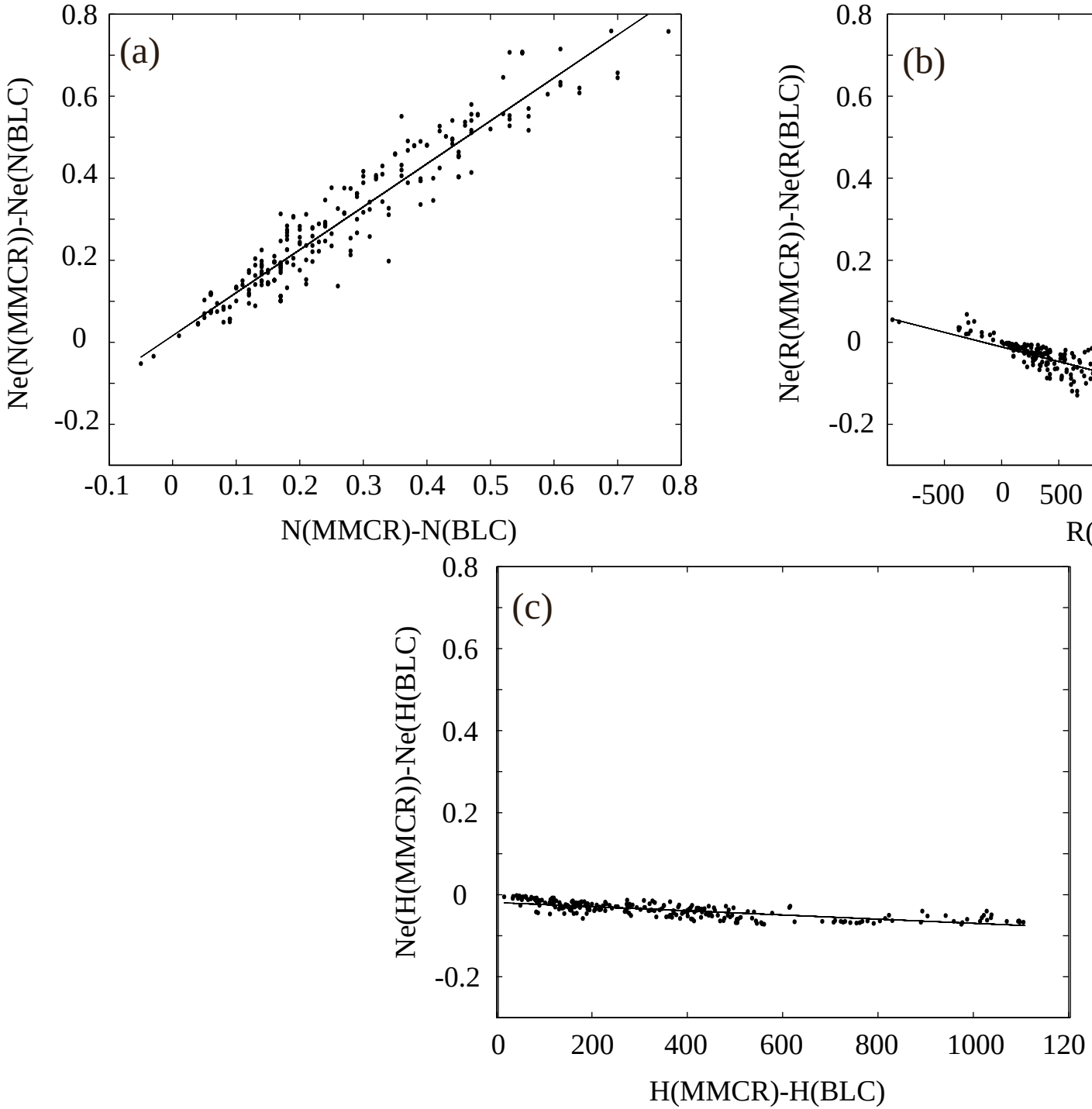

Fig. 10. The effects of (a) different N's (same β), (b) different R's (same N) and different h's (same N) on model calculated Ne's.

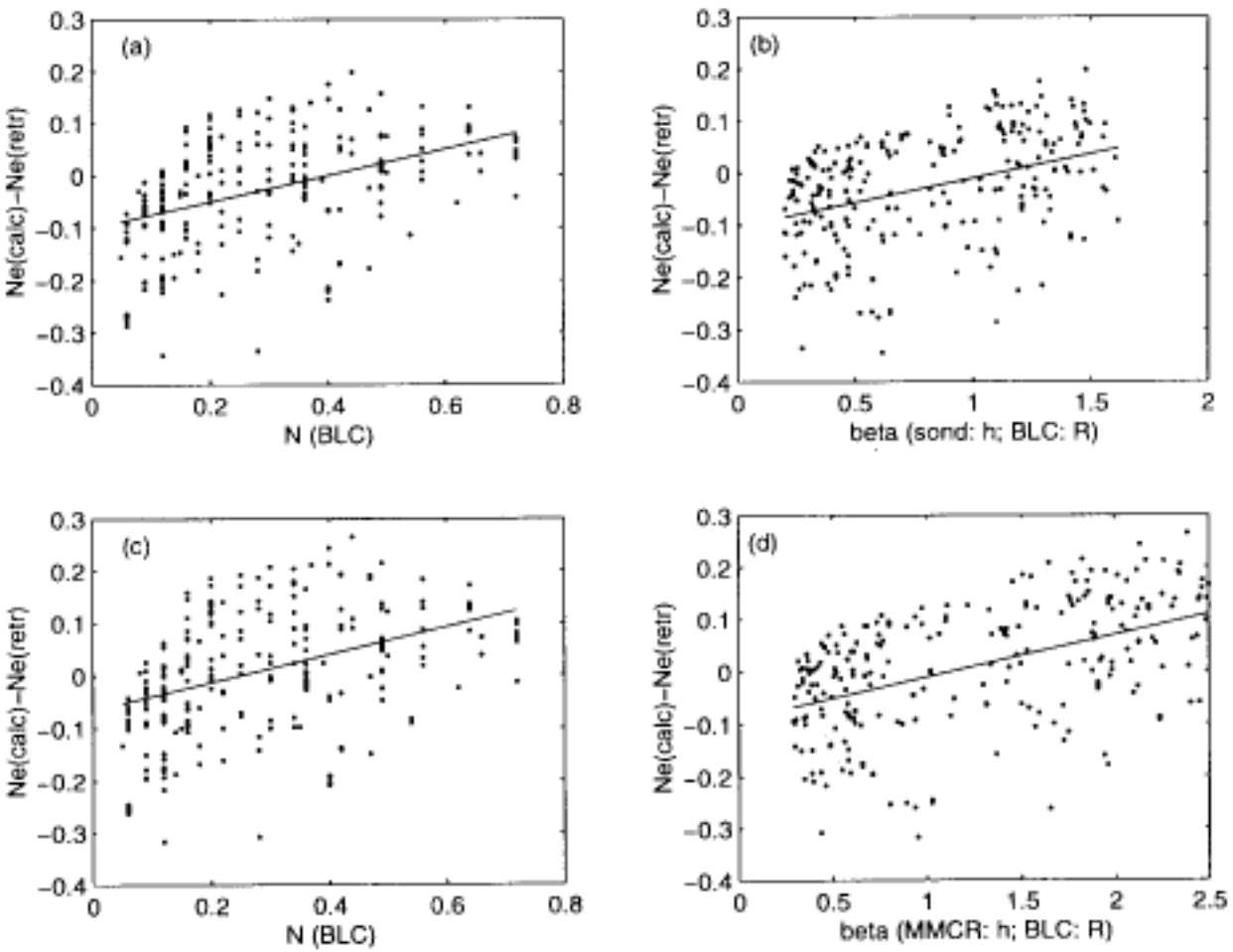

Figure. 11 The dependence of the difference between model calculated and retrieved N_e [N_e(calc)-N_e(retr)] on N_{BLC} [(a) and (b)], β [(c) and (d)]. Noted: N_e(calc) using N_{BLC} and sonde-BLC β as input in (a) and (b), and N_{BLC} and MMCR-BLC β as input in (c) and (d).